



PAPER • OPEN ACCESS

## Charge and spin coupling in magnetoresistive oxygen-vacancy strontium ferrate $\text{SrFeO}_{3-\delta}$

To cite this article: S H Lee *et al* 2016 *New J. Phys.* **18** 093033

View the [article online](#) for updates and enhancements.

### Related content

- [Resonant elastic soft x-ray scattering](#)  
J Fink, E Schierle, E Weschke *et al.*
- [Magnetic ordering and dielectric relaxation in the double perovskite  \$\text{YBaCuFeO}\_5\$](#)   
Yen-Chung Lai, Chao-Hung Du, Chun-Hao Lai *et al.*
- [Double perovskites with ferromagnetism above room temperature](#)  
D Serrate, J M De Teresa and M R Ibarra

### Recent citations

- [Structural, magnetic and electronic properties of pulsed-laser-deposition grown  \$\text{SrFeO}\_3\$  thin films and  \$\text{SrFeO}\_3/\text{La}\_{2/3}\text{Ca}\_{1/3}\text{MnO}\_3\$  multilayers](#)  
E Perret *et al*



## PAPER

Charge and spin coupling in magnetoresistive oxygen-vacancy strontium ferrate  $\text{SrFeO}_{3-\delta}$ 

## OPEN ACCESS

## RECEIVED

13 May 2016

## REVISED

2 September 2016

## ACCEPTED FOR PUBLICATION

5 September 2016

## PUBLISHED

20 September 2016

Original content from this work may be used under the terms of the [Creative Commons Attribution 3.0 licence](#).

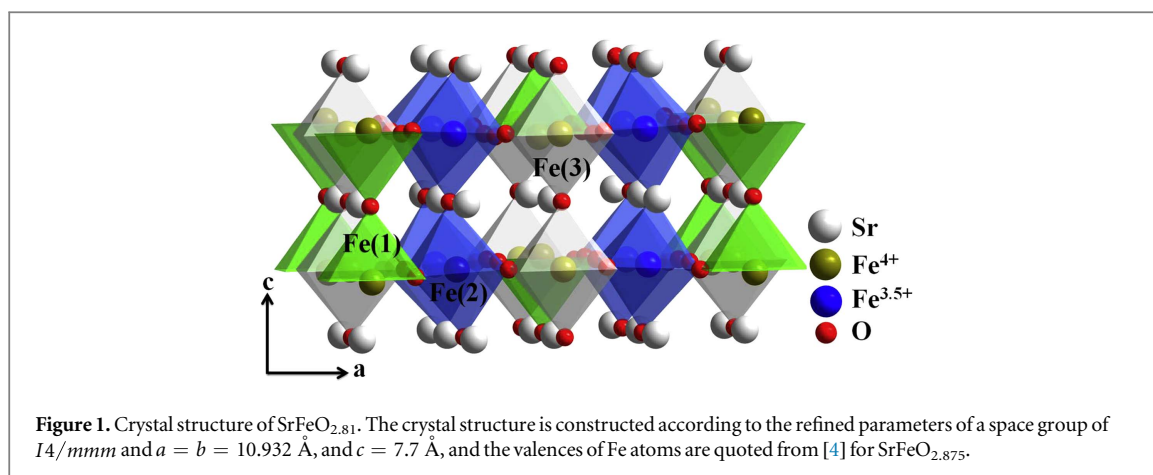
Any further distribution of this work must maintain attribution to the author(s) and the title of the work, journal citation and DOI.

S H Lee<sup>1</sup>, T W Frawley<sup>2</sup>, C H Yao<sup>1</sup>, Y C Lai<sup>1</sup>, Chao-Hung Du<sup>1</sup>, P D Hatton<sup>2</sup>, M J Wang<sup>3</sup>, F C Chou<sup>4</sup> and D J Huang<sup>5</sup><sup>1</sup> Physics Department, Tamkang University, Tamsui 251, Taiwan<sup>2</sup> Department of Physics, Rochester Building, Durham University, Durham DH1 3LE, UK<sup>3</sup> Institute of Astronomy and Astrophysics, Academia Sinica, Taipei 10617, Taiwan<sup>4</sup> Center for Condensed Matter Sciences, National Taiwan University, Taipei 10617, Taiwan<sup>5</sup> National Synchrotron Radiation Research Center, Hsinchu 30076, TaiwanE-mail: [chd@mail.tku.edu.tw](mailto:chd@mail.tku.edu.tw) and [p.d.hatton@durham.ac.uk](mailto:p.d.hatton@durham.ac.uk)**Keywords:** magnetoresistance, charge ordering, spin ordering, resonant x-ray scattering**Abstract**

Using magnetization, conductivity and x-ray scattering measurements, we demonstrate that the giant magnetoresistance of the oxygen-deficient ferrite  $\text{SrFeO}_{2.875 \pm 0.02}$  is a consequence of the coupling between the charge and spin order parameters and the tetragonal to monoclinic structural distortion. Upon cooling the sample at  $T \simeq 120$  K we find a shoulder in both field-cool and zero field cool magnetization data and the simultaneous appearance of incommensurate structural satellites observed using x-ray diffraction. These satellites are shown to be due to incommensurate charge ordering with the high temperature delocalized  $\text{Fe}^{3.5+}$  ions becoming localized with a charge disproportion forming an incommensurate charge-ordered phase. Strong resonant enhancement of these satellites at the Fe  $L_{\text{III}}$  absorption edge confirms that this charge ordering is occurring at the Fe(2) sites. Further cooling increases the charge order correlation until  $T \simeq 62$  K where there is a full structural transition from the tetragonal phase to a monoclinic phase. This causes a jump in the charge order wavevector from an incommensurate value of 0.610 to a commensurate ground state position of 5/8. This first-order structural transition displays considerable hysteresis as well as dramatic reductions in the magnetization, resistivity and magnetoresistance. The transition also causes an antiferromagnetic spin-ordering with a doubled unit cell along the  $c$ -axis. Well as observing new commensurate magnetic reflections at the Fe $_{\text{III}}$  edge we also observed resonant enhancement at the oxygen  $K$ -edge showing considerable hybridization between the Fe 3d and oxygen 2p states at low temperatures. Our results show that the formation of a magnetic long-range ordered ground state drives the charge ordering from an incommensurate ordering to a commensurate ground state. This is evidence of a strong coupling between the magnetic and charge order parameters which is the basis for the unusual magnetoresistive effects observed at the transition.

**1. Introduction**

A wealth of unusual electronic phenomena can emerge in transition metal oxides purely by altering the valence state of the transition metal ion. This subject has been studied extensively in condensed matter physics and has been realized to be one of the key issues in understanding the exotic behavior observed in high- $T_c$  superconductors, multiferroics and magnetoresistive compounds. Among many disparate systems, such as in the cuprates ( $\text{La}_{2-x}\text{Sr}_x\text{CuO}_4$ ,  $\text{YBa}_2\text{Cu}_3\text{O}_7$ ), nickelates ( $\text{La}_{2-x}\text{Sr}_x\text{NiO}_4$ ), manganates ( $\text{La}_{1-x}\text{Ca}_x\text{MnO}_3$ ), and ferrates ( $\text{Fe}_3\text{O}_4$ ,  $\text{BiFeO}_3$ ) the valence states of the transition metal ions can be changed and new valences formed in mixed-valence compounds. Changing the amount of carrier dopants in these systems can cause the valence of the transition metal to change and this results in a rich electronic phase diagram, giving rise to charge, spin and orbital ordering, as well as electronic phase separation.

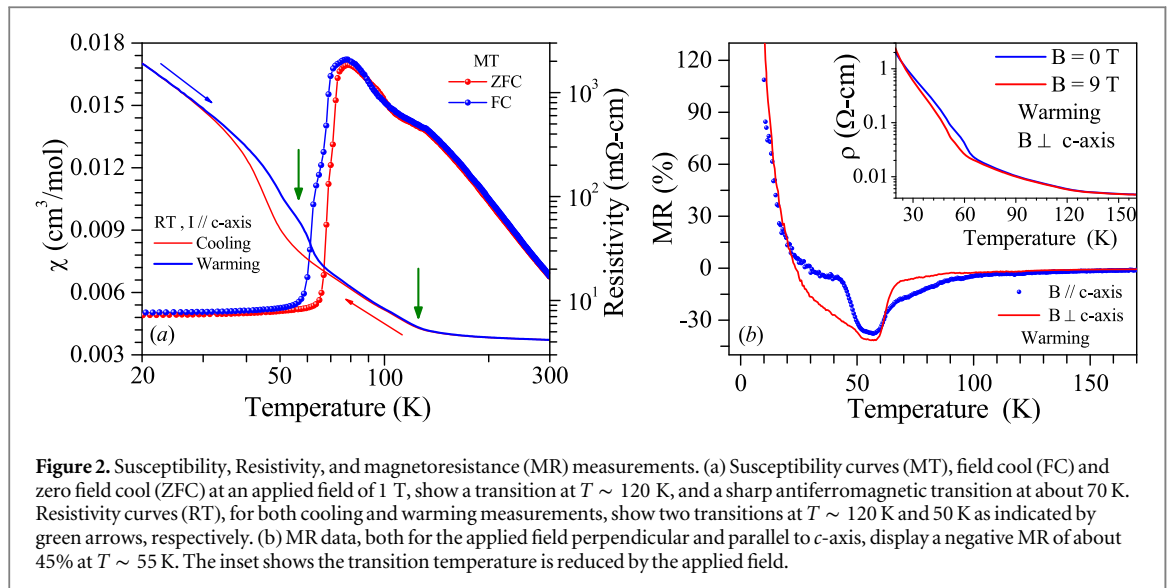


The compound  $\text{SrFeO}_{3-\delta}$  is one such system displaying valence changes, which shows a metal insulator transition and related exotic transport phenomena.  $\text{SrFeO}_{3-\delta}$  describes a family of vacancy ordered perovskite-like structures [1], with the general formula  $\text{Sr}_n\text{Fe}_n\text{O}_{3n-1}$  with known phases of  $n = 2, 4, 8, \infty$  [2, 3]. Above a composition dependent transition temperature the  $\text{SrFeO}_{3-\delta}$  system adopts the cubic structure, with the oxygen vacancies disordered throughout the system. Upon cooling below this transition three miscibility gaps open up, creating four regions with three vacancy-ordered structures [2, 3]. For  $n = \infty$ ,  $\text{SrFeO}_3$  (SFO) has the cubic perovskite structure, containing  $\text{FeO}_6$  octahedra with a valence state of  $\text{Fe}^{4+}$ . Upon reducing the oxygen content,  $n = 8$  and 4 adopt tetragonal and orthorhombic structures, respectively. The  $n = 2$ , material,  $\text{SrFeO}_{2.5}$ , has the brownmillerite-type structure which consists of  $\text{FeO}_6$  octahedra and  $\text{FeO}_4$  tetrahedra, with a valence of  $\text{Fe}^{3+}$ . The end member  $n = 1$ ,  $\text{SrFeO}_2$  is an infinite-layer compound with  $\text{FeO}_4$  squares and has a valence state of  $\text{Fe}^{2+}$  [4, 5]. In certain oxygen concentrations, SFO shows a mixed valence state and giant magnetoresistance. For instance,  $\text{SrFeO}_{2.875}$  ( $\text{Sr}_8\text{Fe}_8\text{O}_{23}$ ) possesses a tetragonal structure at room temperature with three different Fe sites as shown in figure 1, among them, Fe(1) and Fe(3) have been attributed to  $\text{Fe}^{4+}$ , and  $\text{Fe}^{3.5+}$  for Fe(2) [6]. The purpose of this paper is not to provide more information on the properties of this material but rather to investigate the relationship between the structure and its hidden charge and spin orderings. Such a study may provide insights into the origins of the observed properties. In the literature there have been experimental studies of the correlations between the magnetoresistance and the electronic structure of  $\text{SrFeO}_{3-\delta}$ , but many of these studies were limited by the quality of the crystals [6, 7]. Growing oxygen-deficient  $\text{SrFeO}_{3-\delta}$  is technically difficult and often results in a phase-separated mixture of different oxygen deficiencies. This affects bulk measurement techniques such as magnetization and resistivity. Nevertheless, by use of high-resolution x-ray scattering, we will demonstrate it is possible to separate the reflections from different phases, and provide detailed structural information from single crystallites of the material.

## 2. Experimental

For this study, a high-quality single crystal of  $\text{SrFeO}_{3-\delta}$  was grown by the floating-zone method. In order to confirm the crystal structure, a part of the sample was cut and finely ground for a powder diffraction study. Beamline BL01C2 of the NSRRC synchrotron was used, with x-rays of energy 17 keV. The diffraction pattern was recorded on an image plate, and showed a majority phase with a tetragonal unit cell with  $a = b = 10.3931 \text{ \AA}$ , and  $c = 7.7 \text{ \AA}$ , as shown in figure 1. For detailed transport studies, the crystal was first orientated by x-ray diffraction and cut into a thin slab with electrical contacts of gold, 200 nm thick deposited by high-energy sputtering. A Quantum Design PPMS was used to measure the resistance as a function of temperature. A temperature rate of  $2 \text{ K min}^{-1}$  was used for measurements on both warming and cooling. A piece of this sample, of dimensions  $\sim 2 \times 3 \times 1 \text{ mm}^3$  was cut from the grown boule and characterized by x-ray diffraction with the  $\langle 001 \rangle$  as the normal direction. The sample was measured to have a mosaic width of  $\sim 0.11^\circ$  on the structural Bragg peak  $(0, 0, 4)$  at room temperature. The tetragonal unit cell is used throughout this paper and any reciprocal space vectors  $(h, k, l)$  are expressed using this structure.

X-ray diffraction and scattering experiments were performed using the soft x-ray EPU beamline 05B3, and the hard x-ray beamlines BL07 and BL12B2 at NSRRC and SP-8, respectively, and the sample was mounted such that the  $c$ -axis and  $a$ -axis were parallel and perpendicular to the scattering plane. For the experiments done on the beamlines of BL07 and BL12B2, the incident x-ray energy was selected to be 10 keV by a pair of  $\text{Si}(1, 1, 1)$  single crystals and the scattered signal was analyzed by a single crystal of  $\text{LiF}(4, 0, 0)$ . The use of a  $\text{LiF}$  analyzer



crystal, not only improves the experimental resolution, but also helps to separate the diffraction originating from different domains existing in the crystal<sup>6</sup>. By measuring the (0, 0, 4) structural Bragg peak from the sample along different principal directions, the inverse correlation lengths of the sample were determined to be  $\xi_H^{-1} = 0.0197 \text{ \AA}^{-1}$ ,  $\xi_K^{-1} = 0.0069 \text{ \AA}^{-1}$ , and  $\xi_L^{-1} = 0.0022 \text{ \AA}^{-1}$ . This corresponds to a real space correlation length along the  $c$ -axis (the high-resolution direction) of approximate 100 unit cells ( $\sim 770 \text{ \AA}$ ). Such a high real space correlation length suggests that the tetragonal domains are highly ordered and of high crystalline quality. Our x-ray results suggest this sample is overwhelmingly composed of the tetragonal phase ( $\sim 95\%$  tetragonal) with only very minor contributions from any orthorhombic phase.

At the soft x-ray energies available on the EPU beamline, resonant x-ray diffraction (RXD) was performed. The fluorescence spectra of the Fe  $L$  and O  $K$  absorption edges were measured, and the positions of the absorption edges were used to select the incident x-ray energies. The polarization states of the x-rays were chosen to be either parallel ( $\pi$ -polarized) or perpendicular ( $\sigma$ -polarized) to the scattering plane. The diffracted x-rays from the sample were detected by the use of a channeltron detector without an analyzer, and the resolution was defined by a fine rectangular detector slit.

### 3. Results

The powder diffraction measurements show the sample to be made up of a majority phase of the  $n = 8$ , tetragonal  $\text{SrFeO}_{2.875}$  structure, with a 5% unidentified impurity phase<sup>7</sup>. We did not employ techniques such as thermogravimetric analysis of iodometric titration to estimate the oxygen content of our sample. These techniques give an average value with relatively large error bars. Rather we compared the magnetization and resistivity measurements obtained on our sample with those reported by others. In addition we were able to use x-ray techniques to estimate the oxygen composition from the single crystal used. The different oxygen vacancy ordered structures are separated by a miscibility gap, which would indicate that the total oxygen vacancy,  $\delta$  is close to 0.125 with an error from this 5% impurity, leading to  $\delta = 2.875 \pm 0.007$ . The temperature dependence of the susceptibility and resistivity for our sample can be seen in figure 2(a). This shows qualitatively similar behavior to the results reported by Lebon *et al* [8] for a mixed phase sample with overall  $\delta = 0.19$ . This disparity shows the requirement of single phase sample to get useful information from bulk transport measurements, showing the necessity for this study. A sharp transition is observed in the susceptibility data around 70 K, figure 2(a). This is attributed to the antiferromagnetic ordering of the tetragonal  $\text{Sr}_8\text{Fe}_8\text{O}_{23}$  phase. There is hysteresis behavior observed between field-cooling (FC) and zero-FC (ZFC) measurements over this first-order transition. Furthermore, in both the FC and ZFC measurements a kink is observed around 120 K, as shown by the arrow.

<sup>6</sup> According to the literature (PRB 73, 094451, 2006),  $\text{SrFeO}_{2.81}$  could contain a minority orthorhombic phase of  $\text{SrFeO}_{2.75}$ .

<sup>7</sup> We could not identify the existence of the impurity phase on the powder diffraction pattern, but we observed the impurity phase from the single crystal diffraction. Comparison of the intensity of the Bragg peaks the impurity phase is estimated to be less than 5%. The refined parameters cannot tell the structure difference between  $\text{SrFeO}_{2.81}$  and  $\text{SrFeO}_{2.875}$  because of the insensitivity of x-rays to oxygen atoms.

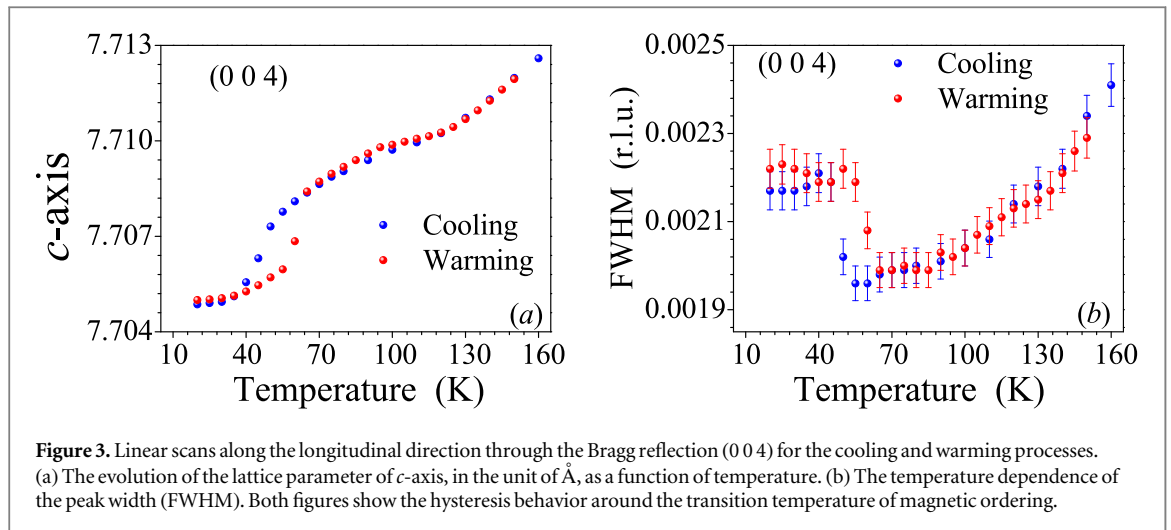


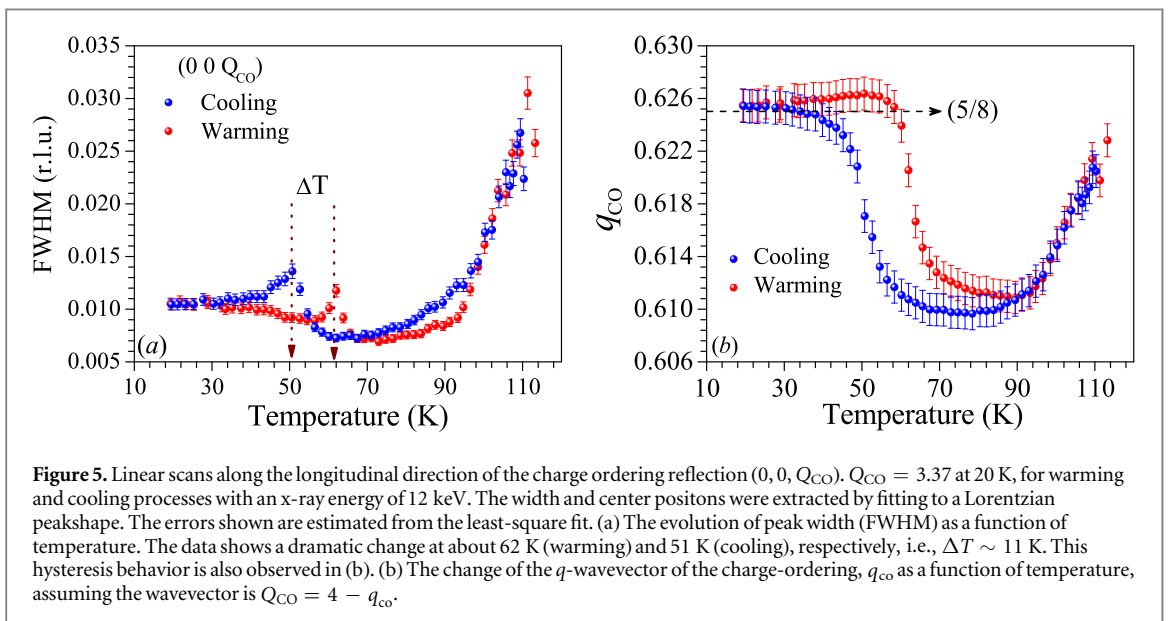
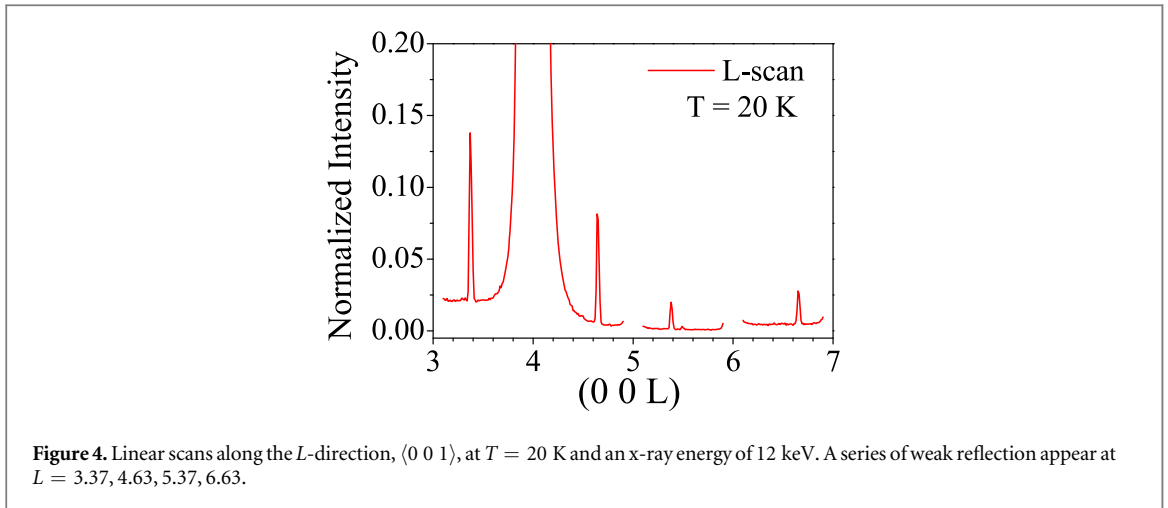
**Figure 3.** Linear scans along the longitudinal direction through the Bragg reflection (0 0 4) for the cooling and warming processes. (a) The evolution of the lattice parameter of  $c$ -axis, in the unit of Å, as a function of temperature. (b) The temperature dependence of the peak width (FWHM). Both figures show the hysteresis behavior around the transition temperature of magnetic ordering.

Resistivity was measured along the  $c$ -axis on both cooling and warming processes, and the results are shown as the blue and red solid lines respectively in figure 2(a). The resistivity behaves linearly with temperature from 300 K, a departure from this behavior occurs around  $T_1 \sim 120$  K. The resistivity increases more rapidly below  $T_1$  on cooling, to  $T_2 \sim 45$  K, at which point the resistivity increases more rapidly, until  $T_3 \sim 35$  K, after which the rate of increase in resistivity is reduced. Thermal hysteresis is observed between 35 and 65 K, with the measurements made on warming having the higher resistivity. To study the magnetoresistance (MR) of the system, resistance was measured on warming with a magnetic field of 9 T, applied both perpendicular and parallel to the  $c$ -axis. Figure 2(b) shows the subsequent MR behavior, with blue and red markers showing the magnetic field applied parallel and perpendicular respectively. The anisotropic behavior observed between these two measurements indicates the existence of a component of the magnetic moment in the  $a$ - $b$  plane. A significant reduction in the resistivity at the AFM ordering temperature is seen under the application of an applied magnetic field, shown in the inset of figure 2(b). This indicates that the AFM ordering temperature is suppressed by the applied magnetic field. Consequently the resistivity demonstrates giant negative magnetoresistance, defined as  $\frac{\rho_H(T) - \rho_0(T)}{\rho_0(T)}$ , near the AFM ordering temperature.

In order to examine the unusual transition at about around 60 K as shown in figure 2(a), x-ray scattering experiments were carried out on this sample using high-energy x-rays of 10 keV. The sample was cooled down to 20 K, and the reciprocal lattice set up in the same tetragonal phase as before using the (0, 0, 4) and (4, 0, 4) Bragg peaks. The (0, 0, 4) Bragg peak from the host lattice was studied on warming and cooling. Reciprocal lattice scans were measured in the high-resolution  $L$ -direction across the (0, 0, 4) Bragg peak. The  $c$ -axis lattice parameter can be extracted from the center position of the reciprocal lattice scan. Figure 3(a) shows the change in  $c$ -axis lattice parameter as a function of temperature. Figure 3(b) displays the temperature dependence of the full-width half-maximum of the  $L$ -scan. The change in the  $c$ -axis lattice parameter with temperature shows the presence of a structural transition around 62 K. Tetragonal  $\text{Sr}_8\text{Fe}_8\text{O}_{23}$  has a documented structural transition from the high temperature tetragonal  $I/4mmm$  to a lower symmetry monoclinic  $I2/m$  space group [9]. An about 11 K wide hysteresis is observed between measurements taken on warming and cooling. This structural transition is also responsible for the peak broadening at about 62 K (for warming) and 51 (for cooling).

A series of weak reflections were observed at positions, (0, 0, 1.37), (0, 0, 2.63), (0, 0, 3.37), (0, 0, 4.63), (0, 0, 5.37), (0, 0, 6.63) etc, as shown in figure 4. After a detailed search and corrected with the lattice parameters<sup>8</sup>, the satellite reflections can be indexed as (0, 0,  $L \pm \epsilon$ ), where  $L$  is even and  $\epsilon \sim 0.625$  at 20 K, which can also be expressed as a  $q$ -wavevector of  $\vec{q} = \frac{2\pi}{c} \left( 0, 0, \frac{5}{8} + \zeta \right)$ , where  $\zeta$  is a temperature dependent value. A detailed study of these structural satellites was performed on the (0, 0, 3.37) reflection. Longitudinal scans through the reflection were taken as a function of temperature upon warming and cooling, red and blue lines respectively, in figures 5(a) and (b). The satellite peak was observed to disappear at 115 K. For around 20 K from when charge order satellite peaks arises, the peaks width rapidly shrinks from 0.03 to 0.01 r.l.u. as the system cools and the correlation of the associated phase increases. The full width at half maximum (FWHM) then shows similar behavior to that of the (0, 0, 4) Bragg peak. At the structural transition  $T \sim 62$  K, there is a maximum in the FWHM, below which the width stabilizes at a larger value, suggesting a transition below which the phase responsible for the satellites is less correlated. The 11 K wide hysteresis is observed in these satellites

<sup>8</sup> After corrections due to the lattice parameters at 20 K, the positions of satellite reflections can be expressed as (0, 0, 1.375), (0, 0, 2.625), (0, 0, 3.375), (0, 0, 4.625), (0, 0, 5.325), etc.



over the structural transition. The wavevector of the satellites peaks is temperature dependent. Figure 5(b) shows the movement of the center of the  $(0, 0, 3.37)$  reflection with temperature, this has been corrected for the change in  $c$ -axis lattice parameter, and so is independent of lattice contraction. The satellite peaks appear at an incommensurate position in reciprocal space, upon cooling the incommensurate wavevector of the reflection decreases linearly until around 90 K where it stabilizes at 0.610 r.l.u. co-incident with the stabilizing of the FWHM. Cooling further and the wavevector position undergoes a sharp transition co-incident with the structural transition seen in the  $c$ -axis, stabilizing at a commensurate position of  $\frac{5}{8}$ . The hysteresis behavior is still present in the satellite peak even after the hysteresis in the  $c$ -axis parameter has been accounted for, indicating this hysteresis is not driven by the structural transition. The co-incident temperatures of this transition with the structural suggest both are driven by the same order parameter. The presence of hysteresis in both the structural and charge-order transitions suggest both are caused by a third order parameter.

In order to investigate the origin of these structural satellites, a resonant soft x-ray diffraction experiment was carried out looking along the  $[00L]$  direction. A huge resonant reflection, at the Fe  $L_3$  edge with  $\sigma$ -polarized x-rays, was observed at the reciprocal lattice position  $(0, 0, 0.63)$  at 20 K, figure 6. An additional reflection was observed on resonance at the reciprocal space position of  $(0, 0, 0.5)$ , shown in figure 7(a). Measurements were carried out by taking reciprocal space scans as a function of energy through the magnetic reflection  $(0, 0, 0.5)$  around the Fe  $L$ -edge and the oxygen  $K$ -edge, i.e.,  $\theta$ - $2\theta$  scans as a function of x-ray energy. At the Fe  $L$ -edge, figure 7(a), the fluorescence spectrum shows two main peaks related to the Fe  $L_3$  ( $2p_{3/2} \rightarrow 3d$ ) and Fe  $L_2$  ( $2p_{1/2} \rightarrow 3d$ ) dipole transitions.

The  $(0, 0, 0.63)$  was found to resonate at a maximum of 713.1 eV, figure 8(b), whereas the  $(0, 0, 0.5)$  reflection was maximized at 714.2 eV. Polarization analysis was carried out on both peaks. High-resolution  $\theta$ - $2\theta$

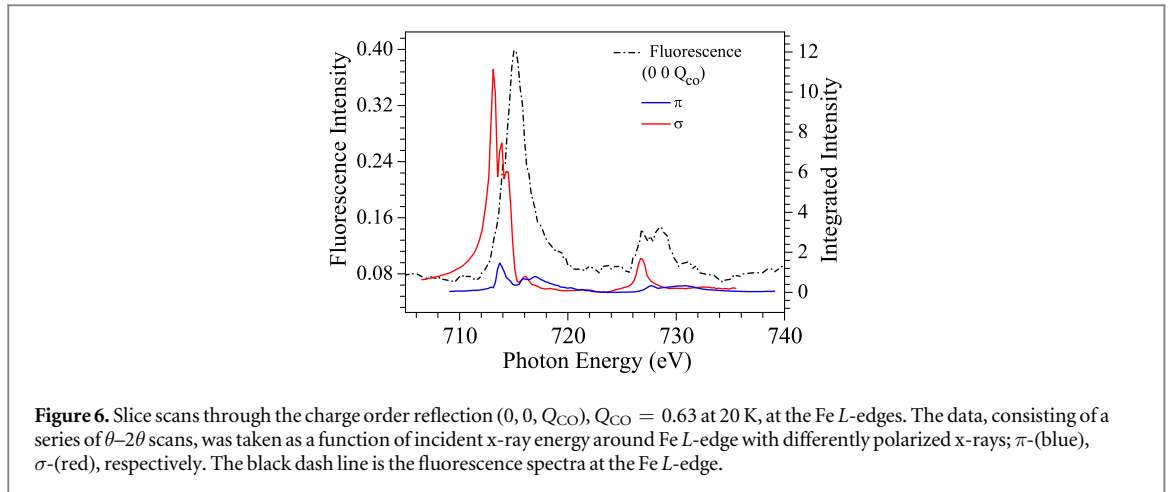


**Figure 6.** Slice scans through the charge order reflection  $(0, 0, Q_{CO})$ ,  $Q_{CO} = 0.63$  at 20 K, at the Fe  $L$ -edges. The data, consisting of a series of  $\theta$ - $2\theta$  scans, was taken as a function of incident x-ray energy around Fe  $L$ -edge with differently polarized x-rays;  $\pi$ - (blue),  $\sigma$ - (red), respectively. The black dash line is the fluorescence spectra at the Fe  $L$ -edge.

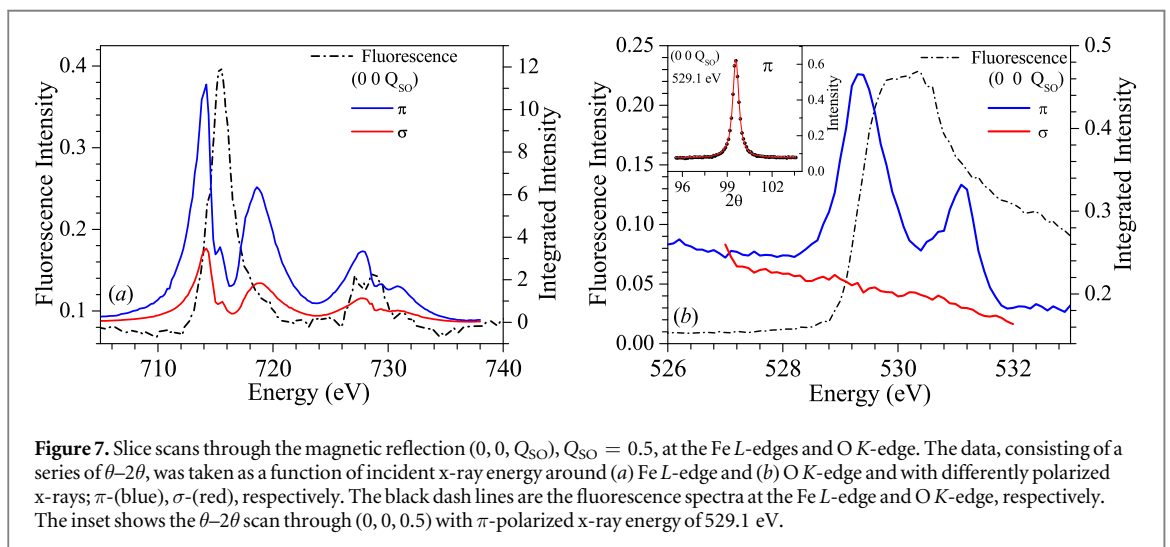


**Figure 7.** Slice scans through the magnetic reflection  $(0, 0, Q_{SO})$ ,  $Q_{SO} = 0.5$ , at the Fe  $L$ -edges and O  $K$ -edge. The data, consisting of a series of  $\theta$ - $2\theta$ , was taken as a function of incident x-ray energy around (a) Fe  $L$ -edge and (b) O  $K$ -edge and with differently polarized x-rays;  $\pi$ - (blue),  $\sigma$ - (red), respectively. The black dash lines are the fluorescence spectra at the Fe  $L$ -edge and O  $K$ -edge, respectively. The inset shows the  $\theta$ - $2\theta$  scan through  $(0, 0, 0.5)$  with  $\pi$ -polarized x-ray energy of 529.1 eV.

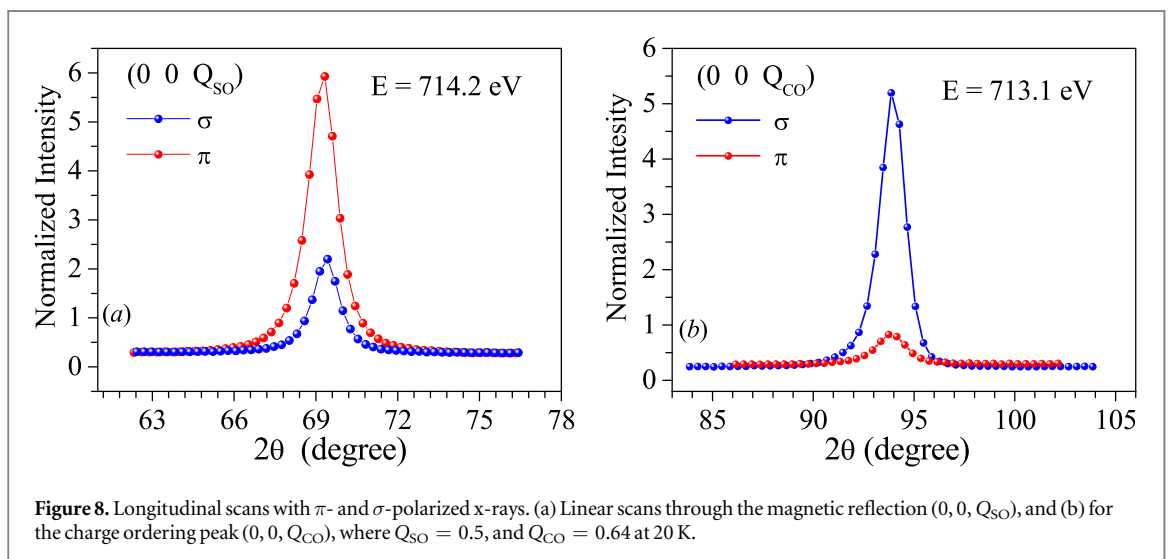
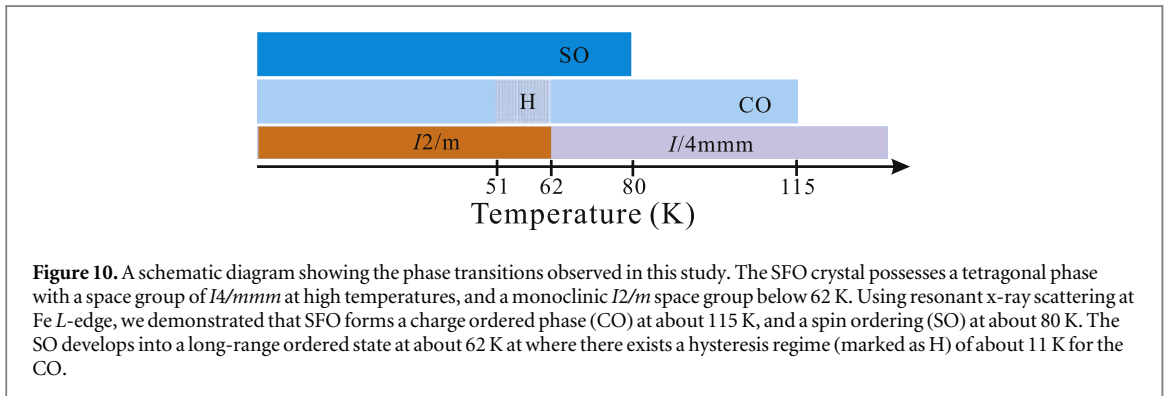
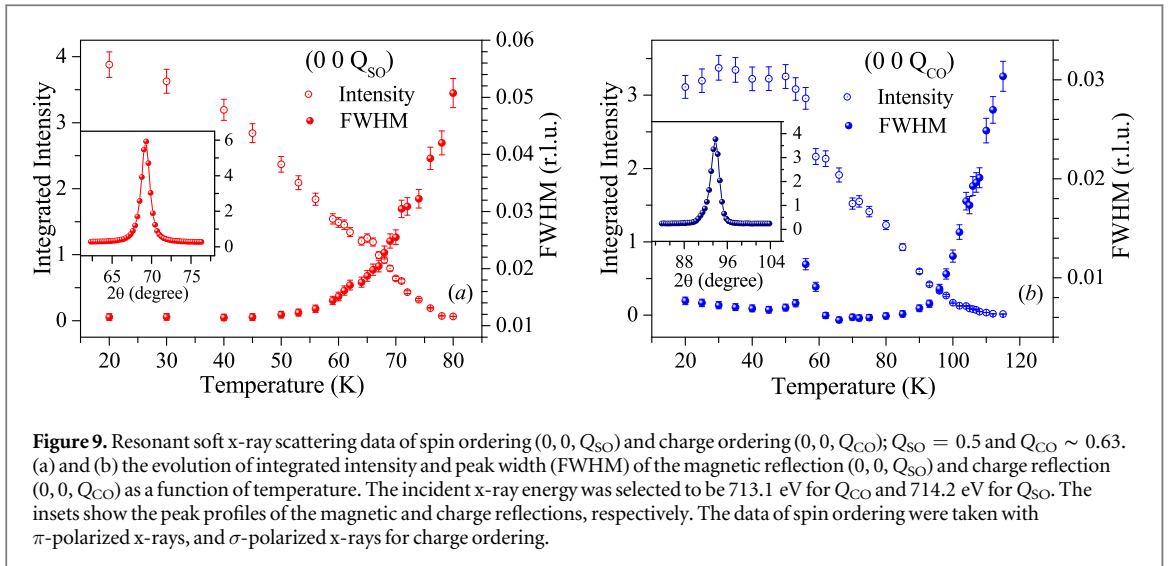


**Figure 8.** Longitudinal scans with  $\pi$ - and  $\sigma$ -polarized x-rays. (a) Linear scans through the magnetic reflection  $(0, 0, Q_{SO})$ , and (b) for the charge ordering peak  $(0, 0, Q_{CO})$ , where  $Q_{SO} = 0.5$ , and  $Q_{CO} = 0.64$  at 20 K.

scans were measured at 20 K, with horizontally ( $\sigma$ ) and vertically ( $\pi$ ) polarized incident x-rays, shown in figure 8. The  $(0, 0, 0.63)$  structural satellites is eight times stronger in the  $\sigma$ -channel than in  $\pi$ , whereas the  $(0, 0, 0.5)$  reflection was three-times stronger in the  $\pi$ -channel than in the  $\sigma$ -channel. Both peaks were also measured as a function of temperature. Reciprocal lattice scans along the  $L$ -direction were measured across the resonant peaks on warming from a base temperature of 20 K. The peaks were fitted with a Lorentzian function. The integrated



intensity and FWHM of the peaks are shown in figure 10. The  $(0, 0, 0.63)$  disappears at 115 K agreeing with the high-energy x-ray study. The FWHM of the  $(0, 0, 0.63)$  shows the same behavior as the high-energy study, with a peak at around 57 K. Co-incident with this feature in the FWHM the integrated intensity stabilizes. The  $(0, 0, 0.5)$  resonant peak disappears at about 80 K. The reflection was measured as a function of temperature, and the peak profile analyzed using a Lorentzian function. The temperature dependence of the integrated intensity of this reflection shows a second-order-like transition, with the integrated intensity of the peak increasing as the temperature cools. The FWHM stays constant from 20 to 50 K about 0.01 r.l.u., after which the width increases, until the peak disappears at 80 K. The  $(0, 0, 0.5)$  was found to resonate at the oxygen  $K$ -edge. Figure 7(b) shows two features in the oxygen resonance resonance.

#### 4. Discussion

The sample used in this study was shown to be comprised of 95% of  $Sr_8Fe_8O_{23}$ . This structure is shown in figure 1 and has three inequivalent Fe sites, Fe(1) on the 4e Wyckoff site in a square-based pyramid oxygen geometry, Fe(2) on the 8f site, in a tilted octahedral geometry and Fe(3) at the 4d site in an octahedral geometry [10]. The resistivity, (figure 2) shows typical semiconductor behavior, with resistivity decreasing with increasing temperature. The first transition at  $T_1$  is coincident with the shoulder in the susceptibility data, as well as the appearance of the structural satellites at  $(0, 0, 0.63)$ . The structural transition that was observed in the measurements of the  $(004)$  Bragg peak, occurs within the 35–45 K region, coinciding with the regime between  $T_2$  and  $T_3$  in the resistivity. The change in  $c$ -axis lattice parameter, qualitatively agrees with that reported by Reehuis *et al* [9], but with a slightly lower transition temperature. Reehuis *et al* found the lower symmetry structure was necessary, as the  $2\theta$  position of large  $l$  reflections above  $130^\circ$  differed slightly from observed positions. The monoclinic space group  $I2/m$ , was found to fit their data best. The main difference between the structures is the splitting of the Fe(2) site along with the corner sharing oxygen sites in the  $a$ - $b$  plane. The differing Fe–O bond lengths caused by the site splitting in the monoclinic symmetry was used to imply charge-ordering on the Fe(2) site from the neutron measurements, which is insensitive to valence state of the iron ion.

It has been suggested that an increase in peak width of the (004) Bragg reflection, at this transition could be due to a lattice distortion from the tilting of the  $\text{FeO}_6$  octahedra [9]. The shoulder in the susceptibility at 115 K has, in the literature, been attributed to helical magnetic order from a residual cubic  $\text{SrFeO}_3$  phase [6, 8]. However, the appearance of the (0, 0, 0.63) satellite peaks at this temperature throws this into doubt. The strong resonant enhancement to the (0, 0, 0.63) structural satellite peaks at the  $\text{Fe } L_{\text{III}}$ , ties their origin to the iron sites. The detector angle,  $2\theta$  of the scattering of the (0, 0, 0.63) reflection on resonance is close to ninety degrees, and for a pure charge origin the  $\pi$ -incidence-channel is expected to be suppressed to less than 1% that of the  $\sigma$ -incidence-channel. The intensity in the  $\pi$ -incidence-channel is 11% of the intensity of the  $\sigma$ -incidence-channel, suggesting an additional contribution to the (0, 0, 0.63) on resonance, possible anisotropic tensor of susceptibility (ATS) scattering.

Mössbauer measurements reported by Adler *et al* [6] and Lebon *et al* [8], show a charge disproportionation transition present in the tetragonal structure. The Fe(2) ions at the 8f Wyckoff site, are reported to have a valency of  $\text{Fe}^{3.5+}$  at room temperature, which has split into  $\text{Fe}^{3+}$  and  $\text{Fe}^{4+}$  by 15 K. This charge disproportionation had been thought to occur at the structural transition to monoclinic, around 50 K for our sample. The charge origin of the satellite peaks suggests this charge disproportionation of the Fe(2) site is in fact the formation of a charge order with an incommensurate wavevector of (0, 0, 0.63), and occurs above the structural transition. The formation of the charge order is a localization of charge carriers on the Fe(2) site, which causes an increase in resistivity, similar to a metal–insulator transition. The Fe(2) ion is magnetically active, and the localization of charge on this site has an effect on the magnitude of the Fe(2) moment, causing the feature in the paramagnetic region of the susceptibility. The appearance of these incommensurate charge-order reflections throws doubt on the simple tetragonal to monoclinic explanation for the structural transition. A proper refinement of powder diffraction data is needed which includes the appearance of the incommensurate charge order. It is clear from figure 5(b) that the charge-ordering has three distinct phases, upon its formation at  $T_1 \approx 115$  K, the wavevector adopts an incommensurate position with respect to the lattice, which decreases linearly with lowering of temperature, in accordance with the behavior of weakly localized charges [11]. This incommensurate position stabilizes around 90 K at  $q_{\text{co}} = (0, 0, 0.610)$ . This is also seen in the width of the charge-order diffraction peaks. The FWHM gives an indication of the correlation length and therefore the domain size of the charge-ordered phase. As expected, at 115 K, where the charge-ordering forms, the charge-order is not particularly correlated. As temperature decreases the charge order becomes more correlated suggesting the formation of large charge-order domains. At the structural transition around 54 K (65 K) the charge order wavevector has a sharp transition from the incommensurate position of 0.610 to the commensurate position of  $q_{\text{co}} = (0, 0, \frac{5}{8})$ . A possible connection may exist between the  $\frac{5}{8}$  wavevector of the commensurate charge-order and the oxygen vacancy of  $\delta = \frac{1}{8}$ .

The commensurate charge order phase, is less correlated than the incommensurate phase in the tetragonal lattice. The commensurate-incommensurate charge-order transition shows hysteresis on warming and cooling. This is similar to the manganite,  $\text{La}_{0.5}\text{Ca}_{0.5}\text{MnO}_3$  where a commensurate–incommensurate charge order transition has been reported [12, 13]. The hysteresis present in the commensurate–incommensurate transition relates this transition to the structural transition from tetragonal to monoclinic. This suggests the unusual transport behavior at 60 K, seen in the resistivity measurements in figure 2(a), is associated with this commensurate–incommensurate charge order transition. Such a phenomenon was also observed in the CMR material  $\text{La}_{0.5}\text{Ca}_{0.5}\text{MnO}_3$ , where a first-order ferromagnetic to antiferromagnetic transition was reported to relate to a commensurate–incommensurate charge-ordering domain transition [12].

For the oxygen non-deficient  $\text{SrFeO}_3$  cubic perovskite parent compound, neutron diffraction [14] and x-ray photoemission spectroscopy [15] have shown the magnetic moment takes the high-spin configuration  $t_{2g}^3 e_g^1$  and a co-operative Jahn–Teller effect is expected. This Jahn–Teller effect has not been observed, and modeling of the Fe 2p core level spectra [15] has shown the presence of a large amount of charge-transfer along the Fe–O bond from the oxygen 2p band to the iron 3d orbitals. The cubic  $\text{SrFeO}_3$  ground state is dominated by a  $d_5L$ , configuration explaining the lack of Jahn–Teller distortions. In  $\text{Sr}_8\text{Fe}_8\text{O}_{23}$  for the Fe(2) site the Fe–O bond along the  $c$ -direction is the shortest [9]. The charge-ordering is likely to occur via a charge transfer hybridization along this Fe–O bond. The magnitude of the charge-ordering cannot be extracted from the x-ray data, but using the results from a published Mössbauer study, a charge-ordering on the Fe(2) site, of  $\text{Fe}^{3+}$  and  $\text{Fe}^{4+}$  can be established at 4 K. The Mössbauer process has a characteristic timescale process of  $10^{-8}$  s, meaning this observed charge ordering of  $\text{Fe}^{3.5+}$  to  $\text{Fe}^{3+}$  and  $\text{Fe}^{4+}$  between room temperature and 4 K, may simply be the slowing of charge transfer to a rate on a timescale  $10^{-8}$  s [16]. The resonant x-ray technique has a characteristic lifetime much smaller than Mössbauer, around  $10^{-16}$  s, allowing sensitivity to the charge transfer. If this charge order is due to a cooperative charge transfer phenomena, it is expected to be through the Fe–O bond, meaning large amount of hybridization is expected between the Fe 3d and O 2p bands.

The temperature dependence of the other resonant satellite peak at (0, 0, 0.5), shows the peak disappears by 80 K. The appearance of this resonant satellite reflection is co-incident with the transition in the magnetic susceptibility measurement, figure 2(a), suggesting a magnetic origin to the peak. The polarization measurement of the (0, 0, 0.5) satellite suggests a more complicated origin than just simply charge. Although a charge origin for the (0, 0, 0.5) reflection would have contributions in both  $\sigma$  and  $\pi$ -channels, if this was the case, the intensity in the  $\sigma$ -channel would be expected to be eight-times stronger than the  $\pi$ -channel for the  $2\theta$  position of the peak. The measurement shows that the intensity in the  $\pi$ -channel is in fact three-times larger than the  $\sigma$ -channel. This polarization dependence of the reflection intensity can be understood within the framework of x-ray resonant exchange scattering [17]. For an electric dipole transition process in a resonant scattering experiment with polarized incident x-rays, and no post scatter polarization analysis the total intensity for the two channels for a magnetic scattering origin can be expressed as the following

$$\begin{aligned} I_\sigma &= z_a^* z_a \cos^2 \theta + z_c^* z_c \sin^2 \theta - \frac{1}{2}(z_a^* z_c + z_a z_c^*) \sin 2\theta \\ I_\pi &= z_a^* z_a \cos^2 \theta + z_c^* z_c \sin^2 \theta + \frac{1}{2}(z_a^* z_c + z_a z_c^*) \sin 2\theta \\ &\quad + z_b z_b^* \sin^2 2\theta \\ I_\pi &= I_\sigma + (z_a^* z_c + z_a z_c^*) \sin 2\theta + z_b z_b^* \sin^2 2\theta, \end{aligned}$$

where  $\theta$  is the scattering angle, and  $z_a$ ,  $z_b$ , and  $z_c$  are the components of the magnetic moment along the  $a$ ,  $b$  and  $c$  crystal axis due to the experimental geometry. Without post-scatter polarization analysis and azimuthal dependences, it is not possible to determine the origin of the satellite to be magnetic, given that ATS scattering origin for the reflection, from the anisotropy of the iron sites, would give a similar polarization dependence. Neutron powder diffraction reported the formation of magnetic reflections in the tetragonal phase, doubling the unit cell along the  $c$ -axis of the crystal lattice [9]. This suggests that the reflection observed in the x-ray diffraction is from a spin modulation in the system. Assuming a magnetic origin, it is clear from the above equations the moment cannot lie collinear along a crystallographic axis, as these would give either zero intensity with  $\sigma$ -light or equal intensity in both channels. The neutron diffraction study by Reehuis *et al* [9] suffered as their samples were a phase separated mixture of the different vacancy ordered SrFeO<sub>3- $\delta$</sub>  structures, but they were still able to identify seven magnetic structures with different wavevectors across the four different crystal structures. Due to the powder nature of their measurements they were unable to assign the  $q_{SO} = (0, 0, 0.5)$  peak to a host lattice as it also indexes up as (0, 0, 0.25) in the cubic lattice. They did, however, resolve the spin structure as a canted antiferromagnetic in the  $a$ - $c$  plane, with a canting angle of 54° with respect to the  $c$ -axis. Due to the tetragonal nature of lattice there is no difference between the  $a$ - $c$  plane and the  $b$ - $c$  plane. These two domains will have moments  $z = (i, 0, -0.24)$  and  $z = (0, i, 0.24)$ , which would lead to ratio of  $I_\pi/I_\sigma$  between 1 and 8 depending on the magnetic domains exposed to the x-ray beam. It is therefore not possible to confirm or rule out this magnetic structure without post-scatter polarization analysis and azimuthal measurements. The temperature dependence of the FWHM shows this transition to be second-order, starting as short-range spin correlations and develops long-range order only at low temperatures, below the structural transition. X-ray diffraction is sensitive to long-range order, and a local probe is necessary to study the short-range spin correlations. A muon spin relaxation technique could be used to study these spin correlations and give more detail to the formation of the long-range order.

In addition to the resonance of the spin ordering at 713.1 eV, it is clear from figure 7(a) that there are multiple features in the resonances at  $L_{III}$  and  $L_{II}$ . The three different inequivalent Fe sites have different valencies and crystal field geometries leading to different orbital splittings and a multiplet ground state, giving rise to the multiple resonances observed [18]. An x-ray resonance experiment on the single valence cubic end member SrFeO<sub>3</sub> would provide a useful qualitative comparison.

The (0, 0, 0.5) reflection also shows a resonance at the oxygen  $K$  edge. This reveals a hybridized band structure between Fe 3d and O 2p states. The resonance at the O  $K$  edge at the same wavevector as the magnetic ordering on the Fe atoms, shows the presence of an orbital magnetic moment on the oxygen, indicating the presence of spin polarized oxygen. This confirms the magnetism is mediated by an indirect exchange mechanism via the oxygen atoms. To get quantitative information out of the resonance spectra *ab initio* calculations are required. An attempt was made using the FDMNES package [20] to simulate the O  $K$  edge resonance. The calculations would not converge for the oxygen vacancy ordered structure or Sr<sub>8</sub>Fe<sub>8</sub>O<sub>23</sub>, but simulations for perovskite SrFeO<sub>3</sub> predict only a single pre-edge feature at the oxygen  $K$  edge. The measured oxygen resonance has two features, potentially due to two different oxygen sites. Further work measuring the oxygen resonance above the structural transition would yield interesting information about the role the structural transition has in the Fe 3d to O 2p hybridization. The difficulty in modeling resonant scattering energy dependences, particular resonances at the  $L_{II/III}$  edges, obviates any quantitative information from being extracted.

The presence of three separate Fe sites, and charge ordering on Fe(2) site, complicates the magnetism in the system. The charge ordering suggests both superexchange and double exchange interactions play a role in the long-range order. The Fe(1) square-based pyramids and Fe(3) octahedra do not share a common oxygen ion, but both share oxygens with the charge-ordered Fe(2) tilted octahedra. The superexchange mechanism drives antiferro-ordering between Fe ions of the same valency, the Fe<sup>4+</sup>. Double exchange mechanism drives ferromagnetic ordering between the Fe<sup>3+</sup> and Fe<sup>4+</sup> ions. These two different exchange mechanisms could be the origin of the two resonant features seen in the energy spectra of the magnetic reflection, although without quantitative modeling this is just speculation. This would create a coupling between the charge and magnetic degrees of freedom, as both the charge-ordering and magnetic-order are mediated by the oxygen anions.

Observations of resonances at the oxygen *K* edge are not new and have been seen before in transition metal oxide materials [21, 22]. In the materials Ba<sub>3</sub>NbFe<sub>2</sub>Si<sub>2</sub>O<sub>14</sub> and TbMn<sub>2</sub>O<sub>5</sub>, resonances at the oxygen *K* edge have been observed [21, 22]. In both cases a single peak, roughly one eV wide was observed, and was used as evidence of an orbital moment on the oxygen atoms. In the case of TbMn<sub>2</sub>O<sub>5</sub>, quantitative modeling was performed using the aforementioned FDMNES package. TbMn<sub>2</sub>O<sub>5</sub> is composed of Mn<sup>3+</sup> in a squared based pyramid coordination and Mn<sup>4+</sup> in an octahedra. Their study found the oxygen resonance could only be replicated with a moment on the Mn<sup>3+</sup> and that if this moment was set to zero, the predicted oxygen resonance went to zero. In this case they concluded the oxygen spin polarization arose purely from hybridization with the Mn<sup>3+</sup>. The two resonance features observed in Sr<sub>8</sub>Fe<sub>8</sub>O<sub>23</sub> could be indicative of hybridization with two different Fe ions.

The second order nature of the magnetic transition indicates that the magnetic-order is the driving force behind both the incommensurate–commensurate charge order transition and the monoclinic structural transition. The appearance of short-range spin correlations around 80 K stabilizes the incommensurate charge-order position with respect to temperature. The onset of long range order for the spin structure around 60 K causes the incommensurate charge order to rapidly lock in to a commensurate value. Such a phenomenon was also observed in the CMR material La<sub>0.5</sub>Ca<sub>0.5</sub>MnO<sub>3</sub>, where a first-order ferromagnetic to antiferromagnetic transition was reported to relate to a commensurate–incommensurate charge-ordering domain transition [12].

The charge ordering is responsible for the unusual transport behavior seen in the resistivity data. Although the charge-ordering exists at temperatures above the onset of magnetic order, the magnetism drives changes in the charge order, indirectly affecting the resistivity. This provides a mechanism to explain the observed magnetoresistance behavior. The transitions in the resistivity data in figure 2(a) line up with the transition in the charge-ordering phase, which in turn are driven by the magnetic order. Put simply, the charge-order localizes charges, causing a reduction in conductivity, explaining the logarithmic increase in resistivity at the onset of charge-ordering. The incommensurate and commensurate charge-order phases have different effects on the amount the resistivity increases.

The application of a magnetic field can suppress or encourage the spin correlations, having an impact on the temperatures of the charge order transitions, depending the direction of applied field. The application of field perpendicular to the *c*-axis causes the transition seen in the resistivity, figure 2(b), to occur at a lower temperature. This resistivity transition has been associated with the commensurate–incommensurate charge order transition, suggesting the application of an applied field perpendicular to the *c*-axis suppress the magnetic ordering temperature and consequently the incommensurate to commensurate charge ordering temperature. The magnetoresistance in the *a*–*b* plane shows similar magnetoresistance behavior to the *c*-axis, with the applied field suppressing the temperature of the transition in the resistivity. The presence of magnetoresistance effects along the *c*-axis and *a*–*b* plane suggests the moment in magnetic order-phase lies between the *c*-axis and *a*–*b* plane.

Repeating the high energy x-ray study of the charge order peaks in a 9 T magnetic field would give a direct confirmation of the effect of the field on the charge-order transitions, providing additional confirmation of the coupling between the charge- and magnetic-order. The resistivity measurement in applied field show the same negative magnetoresistance effects observed by Srinath *et al* for a  $\delta \sim 0.17$  sample [19]. They concluded the negative magnetoresistance is due to double exchange processes, and the positive magnetoresistance at low temperature arises from the opening up of the band gap due to antiferromagnetic interactions. The  $(0, 0, \frac{1}{2})$  resonant diffraction peak observed at the Fe *L*<sub>II/III</sub> confirms the presence of an antiferromagnetic ground state. In addition, observations of the oxygen *K*-edge resonance, verifies indirect exchange mechanisms in Sr<sub>8</sub>Fe<sub>8</sub>O<sub>23</sub> via spin polarized oxygen. This supports arguments made by Srinath *et al* [19] on the underlying nature of the negative and positive magnetoresistance.

## 5. Conclusion

In conclusion, combining x-ray scattering techniques and transport studies, we provide direct evidence that the giant magnetoresistance in oxygen-deficient strontium ferrite SrFeO<sub>3- $\delta$</sub>  is a consequence of the coupling

between the charge- and spin-order parameters to the structural distortion. Figure 10 summarizes the various transitions observed by us. Cooling the tetragonal paramagnetic sample down results in both incommensurate charge order below 115 K and long-range antiferromagnetic reflections below 80 K. The first-order structural phase transition from the tetragonal phase to the low temperature monoclinic ground state is observed at temperatures of either 51 or 62 K depending upon whether cooling or heating. The antiferromagnetic spin-ordering doubles the unit-cell along the  $c$ -axis, and its resonance at the oxygen  $K$ -edge reveals a hybridized bandstructure between Fe 3d and O 2p states. As for the charge modulation, the delocalized  $\text{Fe}^{3.5+}$  become localized states with charge disproportionation of  $\text{Fe}^{3.5\pm\Delta}$ , forming an incommensurate charge-ordered phase. This charge-ordering undergoes a transition to a commensurate ground state of  $\frac{5}{8}$ . The formation of a magnetic long-range ordered ground state drives the charge-order transition to a commensurate ground state. This provides a coupling between the magnetic and charge degrees of freedom, leading to the unusual negative magneto-resistance effects observed.

## Acknowledgments

This project was supported by MOST of Taiwan through the grant Nos. MOST 102-2112-M-032-004-MY3, and MOST 105-2119-M-032-002-MY2. The authors also thank NSRRC for the arrangements of the beam times and the support during the experiment. PDH and TWF also thank the Royal Society for an overseas travel grant.

## References

- [1] Aleksandrov K S and Beznosikov V V 1997 *Phys. Solid State* **39** 695
- [2] Takeda Y, Kanno K, Yamamoto O, Takano M, Nakayama N and Bando Y 1986 *J. Solid State Chem.* **63** 237
- [3] Hodges J P, Short S, Jorgensen J D, Xiong X, Dabrowski B, Mini S M and Kimball C W 2000 *J. Solid State Chem.* **151** 190
- [4] Tsujimoto Y, Tassel C, Hayashi N, Watanabe T, Kageyama H, Yoshimura K, Takano M, Ceretti M, Ritter C and Paulus W 2007 *Nature* **450** 1062
- [5] Seinberg L et al 2011 *Inorganic Chemistry* **50** 3988
- [6] Adler P, Lebon A, Damjanović V, Ulrich C, Bernhard C, Boris A V, Maljuk A, Lin C T and Keimer B 2006 *Phys. Rev. B* **73** 094451
- [7] Zhao Y M, Mahendiran R, Nguyen N, Raveau B and Yao R H 2001 *Phys. Rev. B* **64** 024414
- [8] Lebon A, Adler P, Bernhard C, Boris A V, Pimenov A V, Maljuk A, Lin C T, Ulrich C and Keimer B 2004 *Phys. Rev. Lett.* **92** 037202
- [9] Reehuis M, Ulrich C, Maljuk A, Niedermayer C, Ouladdiaf B, Hoser A, Hofmann T and Keimer B 2012 *Phys. Rev. B* **85** 184109
- [10] Williams G, Hemery E K and McCann D 2009 *Phys. Rev. B* **79** 024412
- [11] Loudon J, Cox S, Williams A J, Attfield J P, Littlewood P B, Midgley P A and Mathur N D 2005 *Phys. Rev. Lett.* **94** 097202
- [12] Chen C H and Cheong S W 1996 *Phys. Rev. Lett.* **76** 4042
- [13] Milward G C, Caldero M J and Littlewood P B 2005 *Nature* **433** 607
- [14] Takeda T, Yamaguchi Y and Watanabe H 1972 *J. Phys. Soc. Japan* **33** 967
- [15] Bocquet A E, Fujimori A, Mizokawa T, Saitoh T, Namatame H, Suga S, Kimizuka N, Takeda Y and Takano M 1992 *Phys. Rev. B* **45** 1561
- [16] Takano M, Okita T, Nakayama N, Bando Y, Takeda Y, Yamamoto O and Goodenough J B 1988 *J. Solid State Chem.* **73** 140
- [17] Hill J P and McMorro D F 1996 *Acta Crystallogr. Sec. A* **52** 236
- [18] Abbate M et al 1992 *Phys. Rev. B* **46** 4511
- [19] Srinath S, Kumar M M, Post M L and Srikanth H 2005 *Phys. Rev. B* **72** 054425
- [20] Bunău O and Joly Y 2009 *J. Phys.: Condens. Matter* **21** 345501
- [21] Scagnoli V, Huang S W, Garganourakis M, Souza de R A, Staub U, Simonet V, Lejay P and Ballou R 2013 *Phys. Rev. B* **88** 104417
- [22] Beale T A W et al 2010 *Phys. Rev. Lett.* **105** 087203